Influence of structural defects on carrier recombination and current gain in an InGaAs/AlGaAs/GaAs heterojunction phototransistor

H. T. Lin and D. H. Rich[a)]

Photonic Materials and Devices Laboratory, Department of Materials Science and Engineering, University of Southern California, Los Angeles, California 90089-0241

O. Sjölund, M. Ghisoni, and A. Larsson

Chalmers University of Technology, Department of Optoelectronics and Electrical Measurements, S-412 96 Göteborg, Sweden

We have studied the influence of structural defects on the spatial variation of radiative and nonradiative recombination in an InGaAs/AlGaAs/GaAs resonant cavity enhanced *npn* heterojunction phototransistor (HPT) structure using cathodoluminescence (CL) and electron beam-induced current (EBIC) imaging. Absorber layers of InGaAs/GaAs multiple quantum wells (MQWs) are used to provide the photosensitivity for light with wavelengths that are transparent to the GaAs substrate. The current gain of the HPT under an applied bias voltage depends on the hole accumulation efficiency in the base and therefore on the hole lifetime. Strain relaxation-induced misfit dislocations in the MQWs are found to create regions of enhanced nonradiative recombination thereby reducing locally the hole accumulation efficiency and current gain. The reduction in the local EBIC signal caused by the dark line defects is less than ~20%, suggesting that misfit dislocations in this sample have a relatively small impact on overall device performance. EBIC and CL are found to be excellent complementary probes of the hole accumulation efficiency and relative recombination rates, owing to the high spatial resolution (~1 μm) of excitation of the electron beam used in these techniques. The temperature dependence of the EBIC and spectrally integrated CL images is examined for $85 \leqslant T \leqslant 300$ K, and reveals that nonradiative recombination in the vicinity of misfit dislocations is predominantly thermally activated with observed spatial variations in lifetime and activation energy. © *1996 American Institute of Physics.* [S0021-8979(96)08110-X]

I. INTRODUCTION

Heterojunction phototransistors (HPT) are being increasingly studied for a variety of applications, particularly in optoelectronic integrated circuits and high-gain infrared detectors for fiber-optic communication.[1–4] The optimum HPT design, in order to achieve high photosensitivity with low dark current, requires that the absorption of light in the emitter and the base regions be minimized,[4] thereby requiring the insertion of lower band gap absorption layers in the collector region.[5] Due largely to the transparent nature of GaAs substrate and the maturity of GaAs-based epitaxial growth techniques, the InGaAs/AlGaAs/GaAs-based system, in which InGaAs/GaAs layers form the absorption region in the collector and AlGaAs/GaAs acts as the emitter-base heterojunction, is a leading candidate for HPTs that can be vertically integrated into parallel optical systems. The carrier collection and transport, however may be affected by strain-induced defects in the absorber caused by the lattice mismatch between $In_xGa_{1-x}As$ and GaAs. After exceeding the critical thickness, misfit dislocations will form and the collection efficiency of photoexcited holes in the base will be reduced from the addition of nonradiative recombination channels. Thus, the InGaAs/GaAs absorber layers must be optimized to be of sufficient thickness to attain high absorption, but also to contain a satisfactorily low defect density. The absorption efficiency and photosensitivity can also be enhanced by incorporating a resonant cavity composed of an AlAs/GaAs distributed Bragg reflector (DBR) structure, in which the resonant wavelength corresponds to the absorption peak of InGaAs absorption layers, i.e., a resonant cavity enhanced HPT (RCE-HPT).[5–10] The RCE-HPT structures allow for vertical integration with two-dimensional arrays of components in parallel optical systems and show potential for applications in telecommunication and optical computing.[9,10]

In an *npn*-type RCE-HPT with an open-base common collector configuration, photogenerated electrons drift towards the collector (i.e., the substrate) and photogenerated holes drift to the *p*-type base layer. The holes accumulating in the base region lower the barrier (i.e., screen the built-in field at emitter-base interface) experienced by the electrons in the emitter, thereby causing electron injection from the wide band gap AlGaAs emitter into the base under a forward bias (as illustrated in Fig. 1). This results in an internal current gain relative to the collector-base photocurrent, provided that the diffusion length of injected electrons is larger than the thickness of the base region. The current gain depends on the hole accumulation efficiency in the base and therefore on the excess carrier lifetime. In such lattice mismatched InGaAs/GaAs structures, as previously noted, misfit dislocations and associated point defects will be generated after a certain critical thickness has been reached. The presence of such structural defects will deleteriously enhance the excess carrier recombination rate and possibly impede carrier transport, thereby lowering the current gain and responsivity.

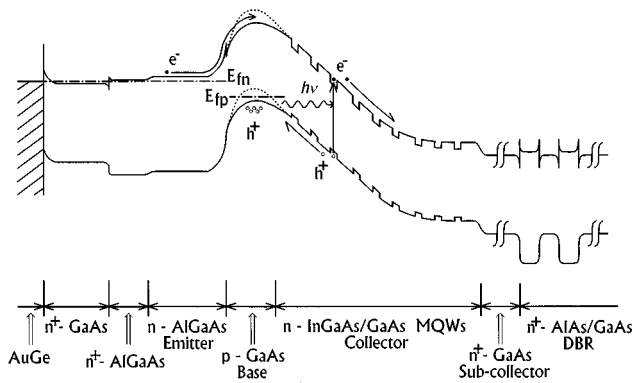[a)]Author to whom correspondence should be addressed.

FIG. 1. Energy band structure of an AlGaAs/InGaAs/GaAs RCE-HPT device in an open-base, common-emitter configuration. Photogenerated electrons drift towards the collector and photogenerated holes drift to the p-type base layer. The accumulation of holes in the base layer causes the reduction in the barrier that electrons in the AlGaAs emitter experience, thereby resulting in internal current gain. The dotted lines indicate the energy band edges prior to excitation.

FIG. 2. Spatially averaged plan-view CL spectra at various temperatures.

Previously, Grundmann *et al.*[11] have measured the reduction of excitonic lifetime in $In_{0.23}Ga_{0.77}As$/GaAs quantum wells (QWs) due to the presence of misfit dislocations using spatially and temporally resolved cathodoluminescence (CL). Rich *et al.*,[12–15] employing a new electron beam induced absorption modulation (EBIA) technique, have quantitatively determined the reduction of excess carrier lifetime and lateral diffusion coefficients in *nipi*-doped InGaAs/GaAs multiple quantum well (MQW) structures caused by the strain relaxation. Little work, however, has addressed the interplay between the carrier recombination rate and collection efficiency of electrically active carriers in strained HPT structures. In this article, we have examined spatial and temperature-dependent variations in (i) the excess carrier recombination using CL imaging and (ii) the collection efficiency of electrically active carriers using electron beam induced current (EBIC) imaging of a strained InGaAs/AlGaAs/GaAs HPT.

II. EXPERIMENT

The HPT was grown by Epitaxial Products International who used low pressure metal-organic chemical vapor deposition on an n^+-GaAs substrate miscut 2° off (100), as previously described.[10] The sample growth was initiated by an n^+-GaAs (3×10^{18} cm^{-3}) buffer layer, after which a high reflectivity n^+-AlAs/GaAs (3×10^{18} cm^{-3}) quarter-wave stack (14.5 pairs; center wavelength corresponding approximately to the absorption peak of 80 Å $In_{0.12}Ga_{0.88}As$/GaAs QWs) was grown. Next, a 3940 Å n^+-GaAs subcollector (3×10^{18} cm^{-3}) and a 4410 Å InGaAs/GaAs MQW collector (5×10^{16} cm^{-3}) were grown. The MQW structure is composed of three groups of three 80 Å $In_{0.12}Ga_{0.88}As$ QWs that are separated by 360 Å GaAs barriers within each group and a center to center spacing of 1325 Å between groups. The $In_{0.12}Ga_{0.88}As$/GaAs MQW structure was designed such that the absorption is insensitive to the growth errors and layer nonuniformities[10] which are essential in a resonant cavity design. Finally, a 1000 Å p-GaAs (5×10^{17} cm^{-3}) base, a
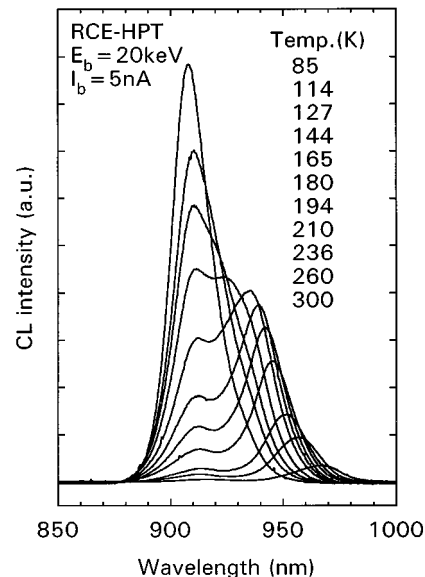
1800 Å n-$Al_{0.3}Ga_{0.7}As$ emitter (5×10^{17} cm^{-3}), a 840 Å n^+-$Al_{0.3}Ga_{0.7}As$ layer (3×10^{18} cm^{-3}), and a 1400 Å n^+-GaAs (3×10^{18} cm^{-3}) contact layer were grown. The energy band diagram is schematically illustrated in Fig. 1. For EBIC experiments, a AuGe/Ni/Au alloy was deposited on the structure surface to form an ohmic contact with the n^+-GaAs contact layer, and subsequently Au wire-bonded for external biasing.

CL and EBIC measurements were performed with a JEOL 840-A scanning electron microscope (SEM). The CL and EBIC system with a temperature variable cryogenic specimen stage were designed and constructed at USC. In CL mode, the luminescence emitted from the sample was collected with an ellipsoidal mirror which focuses the radiation onto an optical fiber bundle leading outside the SEM vacuum chamber to a 25 cm focal length monochromator which was set for a 1 nm total spectral resolution. In EBIC experiments, the sample surface was negatively biased. A 20 keV electron beam was used to generate locally electrons and holes in the base and collector regions, allowing for a field-induced collection of holes in the base. The EBIC signal was detected with a Keithley 428 current amplifier. Thus, the electron beam-induced electron-hole excitation simulates the effects of photoexcitation; with the advantage of a ~1 μm spatial resolution and scanning microscopy capabilities. A liquid nitrogen cooled Ge detector was used to detect the dispersed light during CL experiments.

III. RESULTS AND DISCUSSION

A. CL spectroscopy and imaging of excitonic transitions as a function of temperature

Spatially averaged CL spectra at various temperatures from 85 to 300 K are shown in Fig. 2. The CL spectra of the MQW excitonic ($e1-hh1$) transition in the high temperature range, $T\geq144$ K, exhibit two distinct peaks. The appearance of peaks is an artifact caused by the underlying AlAs/
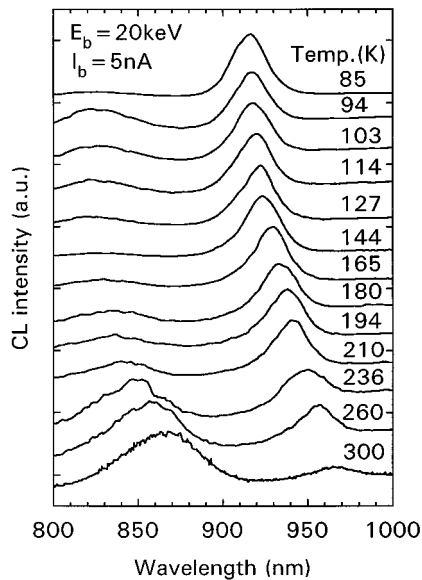
FIG. 3. Spatially averaged cross-sectional CL spectra at various temperatures.

FIG. 4. Transmission at various temperatures.

GaAs DBR which modulates the transmission in the spectral range of the excitonic transition energy. The luminescence line shape without the influence of the underlying AlAs/GaAs DBR can be measured using cross-sectional CL measurements in which a cleaved sample is mounted on a side with its edge facing the electron beam. A single broad peak is observed for the InGaAs/GaAs MQW luminescence for various temperatures, as shown in Fig. 3. The peak position varies from 916 to 965 nm for temperatures ranging from 85 to 300 K. Also, a broad luminescence feature resulting from the GaAs band-edge recombination is observed to move from about 870 to 825 nm as the temperature is decreased from 300 to 85 K. In order to further examine the modulation of light transmitted through the resonant cavity, transmission spectra at various temperatures were also measured, as shown in Fig. 4. In the transmission measurements, a dispersed tungsten light source was coupled into a multimode optical fiber leading to the top surface of the HPT structure in the SEM vacuum system. The positions of dips and peaks in the transmission spectra are consistent with the optical design of this structure.[10] A peak in transmission at $\lambda = 935$ nm at $T = 300$ K agrees with the designed resonant wavelength of 940 nm for device operation.[10] The resonant cavity will have differing effects on the spectral line shape of light which is collected in the CL and transmission measurements (Figs. 2 and 4, respectively), owing to large differences in the source geometry and solid angle of collection in these two experiments.

In order to study the influence of structural defects on carrier recombination at the $In_{0.12}Ga_{0.88}As$/GaAs interfaces, spatially resolved CL was performed. The spatial variation of the spectrally integrated CL (SICL) intensity from the $In_{0.12}Ga_{0.88}As$ QWs at 300 K is shown in Fig. 5(a). In SICL, the integrated MQW excitonic CL intensity is measured in the approximate range $850 \leqslant \lambda \leqslant 1000$ nm. As expected, misfit dislocations and associated point defects cause the reduc-
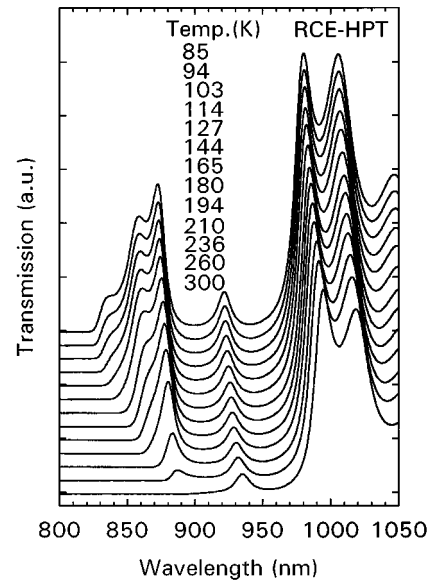
tion of luminescence intensity, thereby giving rise to the formation of dark line defects (DLDs) in the image. Both long and short segments of DLDs running along the high symmetry $\langle 110 \rangle$ directions are observed as a result of the bending of
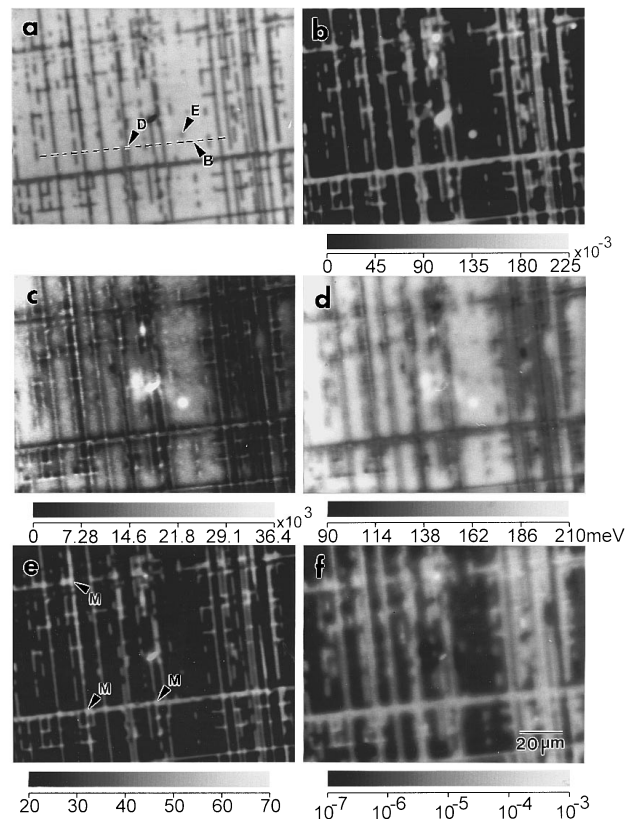

FIG. 5. Spatial imaging of (a) SICL intensity at $T = 300$ K, (b) γ_1, (c) γ_0, (d) E_A, (e) R_{nr}/R_r at $T = 300$ K, and (f) $\gamma_0 \exp(-E_A/kT)$ at $T = 85$ K. The gray keys below (b), (c), (d), (e), and (f) represent the mapping of the ranges as indicted. Bright, dark, and electron beam-bombarded regions denoted as B, D, and E are labeled in (a). The histograms shown in Figs. 6(a), 8, and 11(a) are taken from the line highlighted by the dash line in (a).
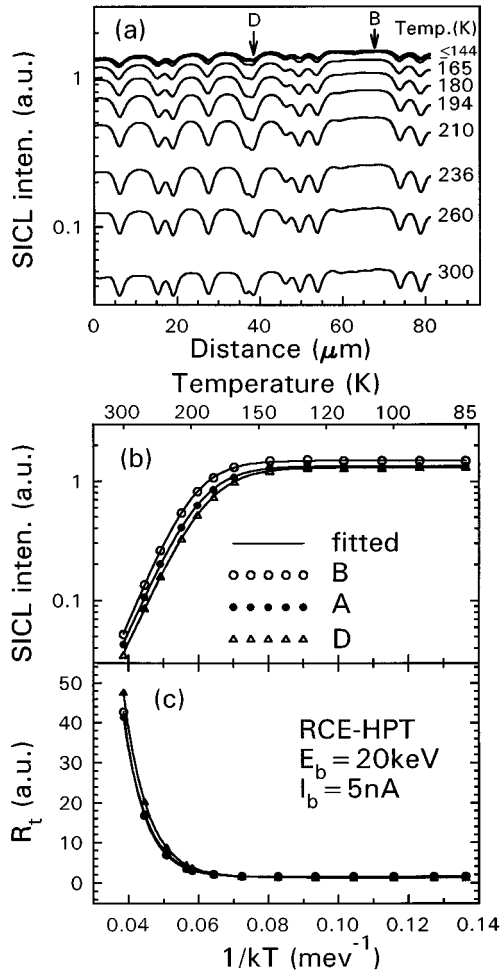
J. Appl. Phys., Vol. 79, No. 10, 15 May 1996

Lin et al. 8017

FIG. 6. (a) Line scanning of SICL intensity along a $\langle 110 \rangle$-oriented direction [highlighted by the dash line in Fig. 5(a)], (b) SICL intensity as a function of $1/kT$, and (c) total recombination rate R_t vs $1/kT$. The data labeled A corresponds to the SICL intensity measured from a spatially averaged region (128 μm×94 μm scanning area). The data labeled B and D correspond to the SICL intensity obtained from a bright and a dark region, respectively, shown in Fig. 5(a). Solid curves in (b) are the fits of Eq. (4) to the data.

threading dislocations at different InGaAs/GaAs interfaces.[16] Figure 6(a) depicts an arbitrary line scan of the SICL intensity along $\langle 110 \rangle$ at various temperatures. Figure 6(b) shows the spatially averaged (labeled A) and spatially localized (fixed electron beam position) SICL intensities in a bright and a dark region (labeled B and D, respectively) plotted vs $1/kT$ (k is the Boltzmann constant), from 85 to 300 K. The SICL intensities reduce by nearly two orders of magnitude as temperature increases from 85 to 300 K. This reduction corresponds to the increase of thermally activated nonradiative recombination, thereby causing an Arrhenius dependence in the high temperature range. In previous reports of the temperature-dependent luminescence efficiency,[17,18] the linear region of the Arrhenius behavior in the high temperature range was characterized by one or two thermally activated nonradiative recombination processes. We use the following fitting equation for the temperature dependence of the SICL intensity:

$$I_{SICL} = R \times \eta, \tag{1}$$

where $\eta = 1/(1 + R_{nr}/R_r)$ is the quantum efficiency,[19,20] R is a coefficient which depends on the generation rate of electron-hole pairs and the relative weights of monomolecular and bimolecular recombination,[19] R_r is the radiative recombination rate which is assumed to be temperature independent, and R_{nr} represents the rate for nonradiative recombination and is assumed to have the following temperature dependence:

$$R_{nr} = R_{nr1} + R_{nr0} \exp(-E_A/kT), \tag{2}$$

where R_{nr0} and E_A are the temperature-independent prefactor and the thermal activation energy,[18,20] respectively, and R_{nr1} is the rate for nonthermally activated nonradiative recombination (i.e., independent of temperature). The temperature-dependent exponential term is due to the enhancement of the capture cross section of nonradiative recombination centers as seen by carriers as the temperature increases. The model of Eq. (2) is motivated by the existence of DLDs in the CL imaging at the lowest temperatures, indicating that there are nonradiative channels which are independent of any thermal activation. Therefore,

$$I_{SICL} = \frac{R}{1 + \gamma_1 + \gamma_0 \exp(-E_A/kT)}, \tag{3}$$

where $\gamma_1 = R_{nr1}/R_r$ and $\gamma_0 = R_{nr0}/R_r$ are temperature independent and proportional to the density of nonthermally and thermally activated nonradiative recombination centers, respectively. At the low temperature limit, η saturates[17,18,20] since thermally activated nonradiative recombination vanishes and I_{SICL} can be approximated as $R/(1 + \gamma_1)$, which accounts for the difference in the spatially localized I_{SICL} at points B and D when $T \leq 144$ K, as shown in Figs. 6(a) and 6(b). Equation (3) can be further reduced to

$$I_{SICL} = \frac{\theta}{1 + \beta \exp(-E_A/kT)}, \tag{4}$$

where $\theta = R/(1 + \gamma_1)$ and $\beta = \gamma_0/(1 + \gamma_1)$. Figure 6(b) shows a fitting of Eq. (4) to the experimental data. It has been previously demonstrated that the dependence of CL intensity on the electron beam current I_b, can facilitate a qualitative determination as to the dominant type of recombination.[21] The results of the SICL intensity dependence on I_b in the HPT structure were examined at two temperatures, 85 and 300 K, and the results are shown in Fig. 7. The SICL intensity is linearly proportional to I_b at $T = 85$ K, whereas a nonlinear behavior, when $I_b \geq 20$ nA, is observed at $T = 300$ K. The linear behavior at 85 K is consistent with the dominance of radiative recombination over nonradiative recombination (i.e., $R_r \gg R_{nr}$).[21] Conversely, the deviation from linearity at $T = 300$ K suggest a reversal in the dominant type of transition occurs (i.e., $R_r \ll R_{nr}$) over a limited current range of $I_b \geq 20$ nA. This behavior is generally consistent with the findings of Kyser and Wittry[21] in which I_{SICL} is proportional to I_b^2 at high excitation conditions when $R_r \ll R_{nr}$.

In order to spatially resolve local variations of the parameters γ_1, γ_0, and E_A, we performed imaging of the SICL intensity at various temperatures between 85 and 300 K. Each 128 μm×94 μm scanning area was discretized into 640×480 pixels. The SICL intensity vs temperature depen-
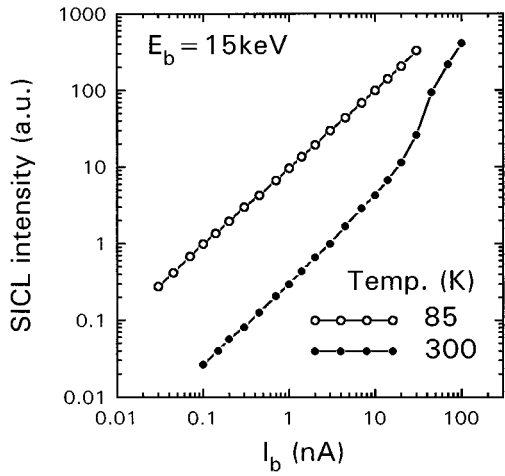
FIG. 7. Spatially averaged SICL intensity as a function of electron beam current I_b at $T=85$ and 300 K.

dence, for each pixel, was fitted according to Eq. (4) to obtain the spatial mapping of θ and β. Since the reduction of luminescence efficiency at low temperature in InGaAs/GaAs MQW structures have been largely attributed to the presence of misfit dislocations and associated point defects,[22] it is our hypothesis that η is approximately unity in the regions away from DLDs, i.e., $\gamma_1 \approx 0$ in the bright regions in Fig. 5(a). Spatial variations in γ_1 can therefore be calculated from the I_{SICL} imaging at $T=85$ K [according to $I_{SICL} \approx \theta = R/(1+\gamma_1)$, where R is assumed to be a constant], and γ_0 is obtained from $\gamma_0 = (1+\gamma_1)\beta$. The results of the fitting for γ_1, γ_0, and E_A are mapped into separate 640×480 images and are shown in Figs. 5(b)–5(d). The gray bars in Figs. 5(b)–5(d) indicate linear scales of γ_1, γ_0, and E_A, which fall in the ranges: $0 \leq \gamma_1 \leq 0.225$, $0 \leq \gamma_0 \leq 36\,400$, and $90 \leq E_A \leq 210$ meV. The spatial variation of γ_1, which is proportional to the nonthermally activated nonradiative recombination rate, is seen in Fig. 5(b) to be correlated (as a reverse contrast) with the pattern of DLDs observed in Fig. 5(a). This indicates an enhancement of nonthermally activated nonradiative recombination processes in the vicinity of DLDs, and is largely due to the increase of density and/or capture cross section of nonradiative recombination centers in the presence of misfit dislocations and associated point defects. A spatial mapping of γ_0, as shown in Fig. 5(c), interestingly reveals a local enhancement along the DLDs seen in Fig. 5(a). The enhancement is easily understood in that γ_0 is proportional to the density of thermally activated nonradiative recombination centers, and is again locally greater along DLDs. Finally, the spatial distribution of E_A is given in Fig. 5(d), in which wide dark bands of gray shade are seen to be associated with DLDs. Figure 5(d) shows that the reduction of E_A can extend ~ 3 μm from the centers of DLDs. This reduction is likely related to the influence of the strain field associated with misfit dislocations and gives rise to local fluctuations of the band edge. Previous studies have attributed the temperature dependence of luminescence in QWs as due to thermal reemission of carriers out of the QWs.[17] We also expect that carrier reemission out of the QWs followed by recombination in the GaAs barriers is operative here since the measured

activation energy of $\sim 150 \pm 50$ meV is close to the sum of the band offsets at the $In_{0.12}Ga_{0.88}As/GaAs$ interfaces (i.e., $\Delta E_V = 48$ meV and $\Delta E_C = 90$ meV).[23] A more complete description of E_A should also include the existence of thermal excitation of deeply trapped excitons or carriers in localized regions followed by nonradiative recombination.

To further illustrate details of the spatial correlation, we show histograms of the SICL intensity at $T=300$ K, γ_1, γ_0, and E_A in Figs. 8(a)–8(d), respectively, vs distance, where the distance was chosen along an arbitrary $\langle 110 \rangle$-oriented line [the same one used in Fig. 6(a)]. The results are shown in Figs. 8(a)–8(d), and the spatial correlation can be categorized into essentially four distinct regions. In region i, as indicated by the vertical solid lines, the centers of DLDs in SICL intensity scan exhibit a strong one-to-one correlation with the maxima, local maxima, and shoulders of γ_1, γ_0, and E_A, respectively. Along the DLDs, a region of misfit dislocations and associated point defects exists, leading to the local enhancement of both γ_1 and γ_0. Quantitatively, γ_1 is much less than $\gamma_0(\gamma_1/\gamma_0 \leq 10^{-5})$, and this is consistent with a general description of the type of nonradiative recombination that is characterized by a thermally activated process.[18–20] In region ii, as indicated by the vertical dashed–dotted lines, the bright regions of the SICL image correlate with the local minima of γ_1 and local maxima of γ_0 and E_A. Grundmann et al. reported that the lateral ambipolar diffusion length of excess carriers in an $In_{0.23}Ga_{0.77}As/GaAs$ QW structure was $\lesssim 1$ μm,[11] and hence we expect that nonradiative recombination of excess carriers generated in region ii ($\gtrsim 5$ μm away from region i) is possibly caused by other types of structural defects different in character or density than that associated with DLDs. In regions far from defects, the principal recombination process is expected to be thermal reemission of carriers from the QWs, followed by both radiative and nonradiative recombination in the barriers since the defect channels associated with dislocations are unavailable. This is consistent with a local maxima of γ_0 and E_A, parameters which describe the thermally activated nonradiative recombination in QWs. In region iii, as indicated by vertical dash lines, all fitted parameters γ_1, γ_0, and E_A appear as local minima which is an opposite behavior to that in region ii, with the exception of γ_1. Figure 8(d) shows that the activation energy E_A tends to be minimized at the regions midway between closely packed misfit dislocations. Note that region iii is closely sandwiched by region i (≤ 2 μm to the nearest region i). Therefore, the strain field associated with misfit dislocations is expected to play an important role in the reduction of E_A. It has been previously reported that local variations in excitonic polarization anisotropy and emission energy caused by the local strain field are found to correlate spatially with DLDs for $In_xGa_{1-x}As$ films grown on misoriented GaAs(001) substrates.[24] Reductions in E_A are expected to be directly related to local potential fluctuations, which can laterally confine the excess carriers generated in this region and prevent the lateral diffusion of carriers into defect-related regions (i.e., the DLDs), resulting in the concomitant reduction of both γ_1 and γ_0. Finally, region iv, as indicated by a vertical dotted line, represents a unique region near a dark spot [labeled E in Fig. 5(a)] caused by electron beam bom-
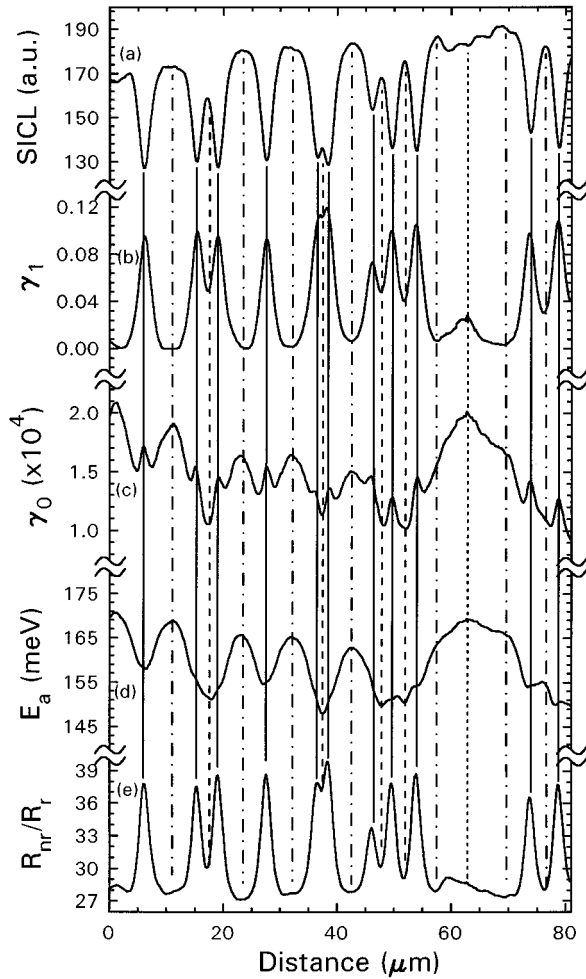
J. Appl. Phys., Vol. 79, No. 10, 15 May 1996

Lin et al.   8019

FIG. 8. Histograms of (a) SICL intensity at $T=300$ K, (b) γ_1, (c) γ_0, (d) E_A, and (e) R_{nr}/R_r at $T=300$ K vs the distance along the line scanning highlighted by the dash line in Fig. 2(a).

FIG. 9. Schematic diagram of EBIC experimental setup.

to ~ 70 in the regions where two orthogonal $\langle 110 \rangle$ DLDs intersect (labeled M in the figure), representing the presence of a higher defect density area. At $T=85$ K, the thermally activated nonradiative recombination is expected to be quenched; therefore, $\gamma_0 \exp(-E_A/kT)$ as shown in Fig. 5(f) is calculated to be $\sim 10^{-3}$ and $\sim 10^{-7}$ in the regions, near and far from DLDs, respectively, as indicated by the corresponding gray bar key. As a result, nonthermally activated nonradiative recombination, R_{nr1}, is primarily responsible for the reduction of SICL intensity in the vicinity of DLDs in the low temperature range. This is consistent with the saturation of the SICL image contrast at lower temperature limit as shown in Fig. 6. The ratio $R_{nr}/R_r \approx \gamma_1$ at 85 K, which, as seen in Figs. 5(b) and 8(b), is $0 < \gamma_1 \lesssim 0.2$. Based on the fitting results of Fig. 6(b), the overall relative recombination rate

$$R_t = R_r + R_{nr} \simeq R\left[1 + \gamma_1 + \gamma_0 \, \exp\left(-\frac{E_A}{kT} \right) \right] \tag{5}$$

can be calculated and the results are shown in Fig. 6(c). R_t in the vicinity of DLDs (i.e., point D in the figure), is largest, as expected, in the high temperature range.

B. EBIC imaging of carrier collection as a function of temperature

The EBIC technique enables a measurement of local fluctuations in the current gain of the HPT caused by strain-induced defects. The experimental setup is schematically shown in Fig. 9. EBIC images and line scans at various temperatures, ranging from 85 to 300 K, were taken of the same region as the CL images described previously. The surface was negatively biased at 1.0 V, and the device is operated in an open-base, common emitter configuration.

EBIC imaging at 300 and 85 K are shown in Figs. 10(a) and 10(b), respectively. Virtually identical DLDs, with a one-to-one spatial correlation with those in the CL imaging of Fig. 5(a) are seen in Fig. 10(a). This suggests the following two possibilities: (i) A local enhancement of nonradiative recombination in the vicinity of misfit dislocations has reduced the excess hole density collected in the base (see Fig. 1), and (ii) local potential fluctuations associated with misfit dislocations have impeded the carrier transport along the epitaxial growth direction, thereby reducing the collector current. A previous EBIC study of a lattice mismatched GaAlPAs/GaAlAs heterojunction has shown the presence of DLDs which have been attributed to the presence of nonradiative channels caused by misfit dislocations.[25] As illus-

bardment (20 keV and 5 nA for ~ 1 h). The structural damage induced by such bombardment results in a different nonradiative recombination process which exhibits local maxima of all parameters γ_1, γ_0, and E_A. Structural damage and chemical changes can possibly result from the formation of vacancy and interstitial sites, atomic interdiffusion between InGaAs and GaAs layers, and formation of carbon impurities near the surface region caused by carbidization of the surface during beam exposure.

Based on the spatial distribution of γ_1, γ_0, and E_A, the temperature dependent nonradiative to radiative recombination ratio can be constructed, since $R_{nr}/R_r = \gamma_1 + \gamma_0 \exp(-E_A/kT)$. The spatial mapping and histogram of R_{nr}/R_r at the temperature of $T=300$ K are shown in Figs. 5(e) and 8(e), respectively. Figure 5(e) reveals a strong spatial correlation with Fig. 5(a) with a reverse intensity contrast. A base line average of $R_{nr}/R_r \approx 27$ and local maxima of R_{nr}/R_r ranging from 33 to 40 in the vicinity of DLDs are seen in Fig. 8(e), thus indicating nonradiative recombination is the dominant process at $T=300$ K even in regions absent of misfit dislocations, consistent with the conclusions drawn from the data of Fig. 7. By a careful examination of Fig. 5(e), it is evident that the R_{nr}/R_r ratio increases
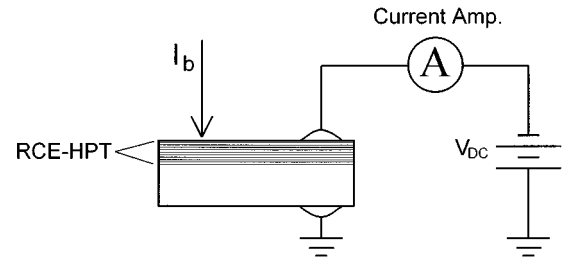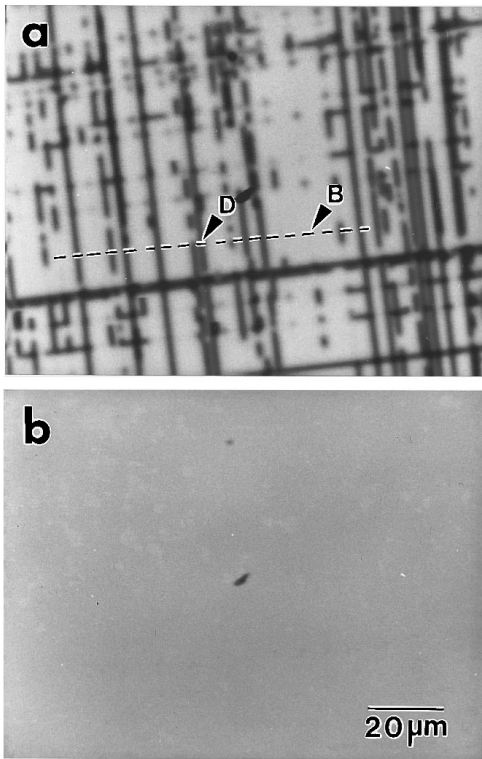
FIG. 10. EBIC imaging at (a) $T = 300$ K and (b) $T = 85$ K. The same spatial area is chosen as that in Fig. 2.

FIG. 11. (a) Line scanning of EBIC at various temperatures, 85 K $\leq T \leq 300$ K. (b) EBIC vs $1/kT$. The labelling denotes the same spatial regions specified in Figs. 2, 3, and 7.

trated in the previous section [in Fig. 6(c)] the total recombination rate R_t is greater near misfit dislocations, suggesting that additional nonradiative channels must be present. As shown in Fig. 6(c), the overall recombination rate drops nearly two orders of magnitude when lowering the temperature from 300 to ≤ 144 K as a result of quenching of nonradiative recombination. The temperature dependence of the EBIC imaging is illustrated in Fig. 10. The contrast in the images in the vicinity of the misfit dislocations vanishes as the temperature approaches 144 K. The absence of a detectable DLD network at 85 K further corroborates with the interpretation of the CL results, as the nonradiative recombination rate becomes vanishingly small at low temperatures. This suggests that the collection of excess holes in the base and transport of carriers which contribute to the collector (EBIC) current are negligibly affected by the misfit dislocations at low temperatures, and further underscores the importance of thermal activation in nonradiative recombination at high temperatures.

To further illustrate the temperature dependence of EBIC, the results of a line scan along the same $\langle 110 \rangle$-oriented line chosen in Fig. 8 are shown in Fig. 11(a). The spatially averaged EBIC signal (labeled A) and local EBIC signals in bright and dark regions (labeled B and D, respectively) as a function of temperature are shown in Fig. 11(b). A decrease in the EBIC signal as T decreases is observed and is attributed to the temperature dependence of the resistivity in the GaAs substrate. The relative change in EBIC between local points B and D in Fig. 11 allows for a qualitative analysis of the defect-induced contribution to the impedance as a function of temperature. The ratio of $\Delta I_c (\Delta I_c = I^B - I^D,$
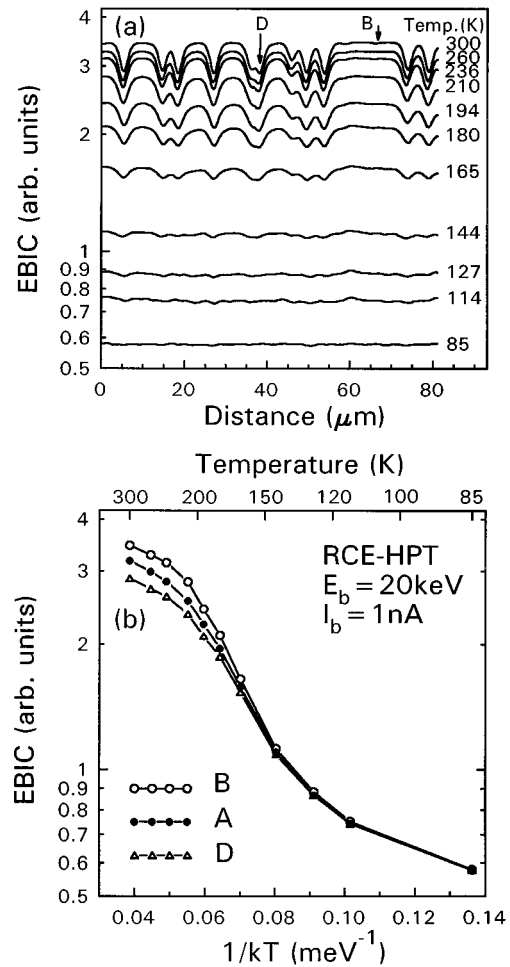
where I^B and I^D are the EBIC at local points B and D, respectively) to $I_c(\sim I^B)$ as a function of $1/kT$ is shown in Fig. 12. The reduction of $\Delta I_c/I_c$ with decreasing temperature reflects the marked reduction in the nonradiative recombination rate in close proximity to DLDs in agreement with the CL results. Conversely, at the high temperature limit, nonradiative recombination is dominant, thereby causing a saturation of $\Delta I_c/I_c$, as observed in Fig. 12. Thus, this EBIC analysis further confirms the strong temperature and spatial dependence of R_{nr}. This influence of dislocations on current gain in this HPT is therefore observed to be minimized when the device is operated at low temperatures. Even at room temperature $\Delta I_c/I_c \lesssim 0.2$, and the overall impact of misfit dislocations on the device performance is relatively small. For a spatially averaged EBIC, the expected defect-induced reduction of the collector current is therefore ~ 0.2 for a linear dislocation density of 10^4 cm^{-1}, or 1 dislocation per μm since the minority carrier diffusion length is ~ 1 μm. For, the present sample, an estimated average linear dislocation density of $\sim 1.5 \times 10^3$ cm^{-1} (as observed in Figs. 5 and 10) scales into a 3% defect-induced reduction of the collector current. Therefore, for related HPT structures in general, when the dislocation density is kept sufficiently small ($\sim 10^3$
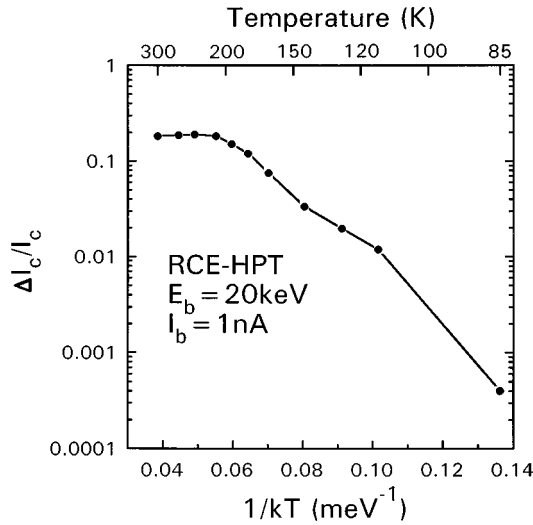
J. Appl. Phys., Vol. 79, No. 10, 15 May 1996

Lin *et al.*   8021

FIG. 12. Variance in EBIC between local points B and D as a function of $1/kT$.
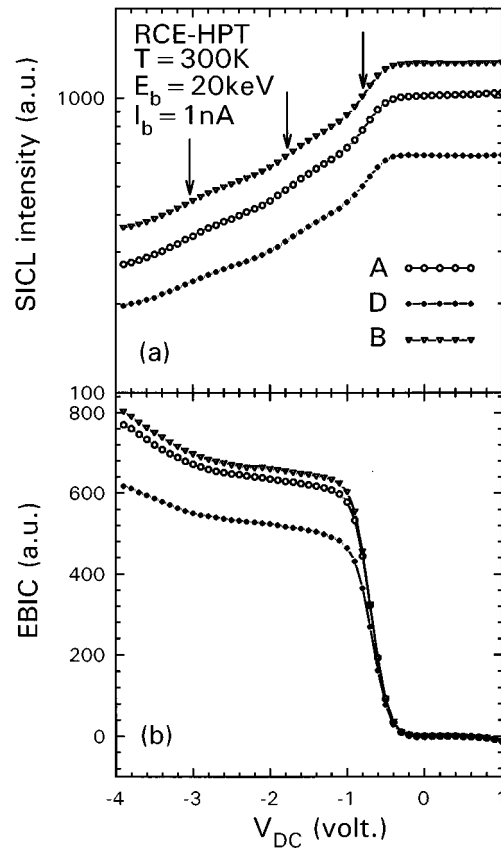

FIG. 13. (a) SICL intensity and (b) EBIC as a function of external dc bias, V_{dc}. Spatial regions labeled A, B, and D are the same as defined previously.

cm^{-1}) and below the density at which dislocation pileups occur, an optimum device performance can be expected.

C. SICL intensity and EBIC as a function of external bias

In order to study the complementary behavior of the carrier capture efficiency of QWs and carrier collection efficiency under a bias voltage, we have performed SICL intensity and EBIC measurements as a function of the bias at $T=300$ K. The results are shown in Fig. 13. The SICL intensity and EBIC were taken from a spatially averaged, a localized bright, and a localized dark area (labeled A, B, and D, respectively) which are the same spatial regions as that chosen in Secs. III A and III B.

With increasing negative bias, the depletion layer at the base/collector interface expands mainly into the InGaAs/GaAs MQWs collector, due to a higher doping concentration in the base than in the collector. Since electrons and holes drift in opposite directions in the depletion region, the carrier capture efficiency by QWs and the excess carrier recombination rate therein is expected to be lower as compared to that in a neutral (low-field) region. Figure 13(a) shows a nearly exponential decrease of SICL intensity when negative bias V_{dc} exceeds ~ 0.4 V. The rate of reduction in the SICL intensity vs V_{dc} is spatially independent, i.e., the relative spatial variation in luminescence efficiency is not influenced by V_{dc}. A steplike behavior in the SICL intensity vs V_{dc} is seen in Fig. 13(a), as indicated by the arrows. Each arrow apparently corresponds to the expansion of the depletion width boundary through an InGaAs QW as the voltage is increased. This causes a steplike change in the rate of carrier capture and recombination efficiency in the QW that is located near the depletion width edge.

The dependence of the EBIC signal as a function of negative bias is shown in Fig. 13(b). Chand et al.[4] have shown, using models, that the current gain and photosensitivity in an HPT increases with the depletion layer thickness.

However, the deleterious influence of structural defects on current gain and photosensitivity were not taken into account. In Fig. 13(b), the deviation in EBIC vs V_{dc} curves (which resemble the photocurrent vs V_{CE} curve for an HPT device) at local regions, B and D, shows that the current collected at all operating voltages is reduced by the presence of dislocations. Again, this is attributed to the enhancement of nonradiative recombination rates and a reduction of carriers active in transport. Thus the voltage dependence of SICL and EBIC imaging quantitatively reveals the deleterious influence of the misfit dislocations in this HPT.

IV. CONCLUSION

Using CL and EBIC, we have studied details of radiative and nonradiative recombination in a partially relaxed AlGaAs/InGaAs/GaAs HPT device. By using an empirical model of the thermally activated nonradiative recombination, which describes the temperature dependence of the CL intensity, the spatial variations of both radiative and nonradiative recombination are quantitatively examined. The thermally activated nonradiative recombination can be characterized by an activation energy, E_A, which is most likely attributed to the formation of trapped carriers followed by nonradiative recombination. The ratio of the nonradiative to radiative recombination rate at 300 K in regions where orthogonal $\langle 110 \rangle$-oriented misfit dislocations intersect is enhanced by a factor of ~ 2.6 ($=70/27$) relative to regions free

of misfit dislocations. In EBIC imaging, a one-to-one spatial correlation of DLDs with CL imaging is observed at 300 K as a result of the enhancement of nonradiative recombination and a reduction of carriers active in transport. The spatial variation in EBIC, however, vanishes at lower temperatures, where the thermally activated nonradiative recombination is quenched. The defect-induced reduction in EBIC was found to be only $\sim$20%, suggesting that an optimized HPT performance can be achieved even with misfit dislocation densities of $\sim 10^3$ cm^{-1}. Therefore, by employing CL and EBIC imaging experiments, we have quantitatively studied the interplay between the formation of strain-induced dislocations, excess carrier recombination, collection and transport in an HPT.

ACKNOWLEDGMENTS

[1] Y. Wang, E. S. Yang, and W. I. Wang, J. Appl. Phys. **74**, 6978 (1993).
[2] L. Y. Leu, J. T. Gardner, and S. R. Forrest, J. Appl. Phys. **69**, 1052 (1991).
[3] A. Dodabalapur and T.-Y. Chang, IEEE Trans. Electron Device Lett. **12**, 693 (1991).
[4] N. Chand, P. A. Houston, and P. N. Robson, IEEE Trans. Electron Devices **ED-32**, 622 (1985).
[5] M. S. Ünlü, K. Kishino, J-I. Chyi, L. Arsenault, J. Reed, and S. Noor Mohammad, Appl. Phys. Lett. **57**, 750 (1990).
[6] M. S. Ünlü, K. Kishino, H. J. Liaw, and H. Morkoc, J. Appl. Phys. **71**, 4049 (1992).
[7] R. P. Bryan, G. R. Olbright, W. S. Fu, T. M. Brennan, and J. Y. Tsao, Appl. Phys. Lett. **59**, 1600 (1991).
[8] F. Y. Huang, A. Salvador, X. Gui, N. Teraguchi, and H. Morkoc, Appl. Phys. Lett. **63**, 141 (1993).
[9] O. Sjölund and A. Larsson, IEEE Photonics Technol. Lett. **7**, 682 (1995).
[10] O. Sjölund, M. Ghisoni, and A. Larsson, Electron. Lett. **31**, 917 (1995).
[11] M. Grundmann, J. Christen, D. Bimberg, A. Fischer-Colbrie, and R. Hull, J. Appl. Phys. **66**, 2214 (1989).
[12] D. H. Rich, K. Rammohan, Y. Tang, H. T. Lin, J. Maserjian, F. J. Grunthaner, A. Larsson, and S. I. Borenstain, Appl. Phys. Lett. **63**, 394 (1993).
[13] D. H. Rich, K. Rammohan, Y. Tang, H. T. Lin, J. Maserjian, F. J. Grunthaner, A. Larsson, and S. I. Borenstain, J. Vac. Sci. Technol. B **11**, 1717 (1993).
[14] D. H. Rich, K. Rammohan, Y. Tang, H. T. Lin, J. Maserjian, F. J. Grunthaner, A. Larsson, and S. I. Borenstain, Appl. Phys. Lett. **64**, 730 (1994).
[15] D. H. Rich, H. T. Lin, and A. Larsson, J. Appl. Phys. **77**, 6557 (1995).
[16] N. Hamaguchi, T. P. Humphreys, D. J. Moore, C. A. Parker, S. M. Bedair, J. C. L. Tarn, G.-L. Jiang, N. EL-Masry, Z. J. Radzimski, and G. A. Rozgonyi, J. Cryst. Growth **93**, 449 (1988).
[17] U. Jahn, J. Menniger, R. Hey, and H. T. Grahn, Appl. Phys. Lett. **64**, 2382 (1994).
[18] J. D. Lambkin, L. Considine, S. Walsh, G. M. O'Connor, C. J. McDonagh, and T. J. Glynn, Appl. Phys. Lett. **65**, 73 (1994).
[19] B. G. Yacobi and D. B. Holt, J. Appl. Phys. **59**, R1 (1986).
[20] J. I. Pankove, *Optical Processes in Semiconductors* (Dover, New York, 1971), p. 166.
[21] D. F. Kyser and D. B. Wittry, in *The Electron Microprobe*, edited by T. D. McKinley, K. F. J. Heinrich, and D. B. Wittry (Wiley, New York, 1964), p. 691.
[22] D. H. Rich, T. George, W. T. Pike, J. Maserjian, F. J. Grunthaner, and A. Larsson, J. Appl. Phys. **72**, 5834 (1992).
[23] S. Niki, C. L. Lin, W. S. C. Chang, and H. H. Wieder, Appl. Phys. Lett. **55**, 1339 (1989).
[24] K. Rammohan, Y. Tang, D. H. Rich, R. S. Goldman, H. H. Wieder, and K. L. Kavanagh, Phys. Rev. B **51**, 5033 (1995).
[25] P. M. Petroff, R. A. Logan, and A. Savage, Phys. Rev. Lett. **44**, 287 (1980).

J. Appl. Phys., Vol. 79, No. 10, 15 May 1996

Lin *et al.* 8023